Electronic Supplementary Information†

On the origin of chaotrope-modulated electrocatalytic activity of Cytochrome *c* at electrified aqueous|organic interfaces†

Alonso Gamero-Quijano,*[ab] Pierre-André Cazade,[ac] Shayon Bhattacharya,[ac] Sarah Walsh,[b] Grégoire Herzog,[d] Damien Thompson*[ac] and Micheál D. Scanlon*[abe]

[a] The Bernal Institute, University of Limerick (UL), Limerick V94 T9PX, Ireland

[b] Department of Chemical Sciences, School of Natural Sciences, University of Limerick (UL), Limerick V94 T9PX, Ireland

[c] Department of Physics, School of Natural Sciences, University of Limerick (UL), Limerick V94 T9PX, Ireland

[d] Laboratoire de Chimie Physique et Microbiologie pour les Matériaux et l'Environnement, Université de Lorraine, CNRS, LCPME, F-54000 Nancy, France

[e] Advanced Materials and Bioengineering Research (AMBER) Centre, Dublin, Ireland

*Corresponding authors:

E-mail: daniel.gamero@ua.es (A.G.-Q.)

E-mail: damien.thompson@ul.ie (D.T.)

E-mail: micheal.scanlon@ul.ie (M.D.S.)

Table of Contents

Movie S1: Molecular dynamics simulation in the presence of urea with the Met80–heme bond intact, a mobile loop spanning residue positions 40–57 in Cyt *c* flips to create a more open structure that increases the accessibility of the heme pocket at the interface.

S1. Supplementary experimental materials and methods

S1.1 Materials. All chemicals were used as received without further purification. All aqueous solutions were prepared with ultra-pure water (Millipore Milli-Q, specific resistivity 18.2 MΩ·cm). The organic solvent α, α, α–trifluorotoluene (TFT, 99+%) was received from Acros Organics. Decamethylferrocene (DcMFc, 97%), guanidinium chloride for molecular biology (GdmCl, ≥ 99%), urea (99.3%), bis(triphenylphosphoranylidene) ammonium chloride (BACl, 97%), tetraethylammonium chloride (TEACl, ≥ 98%) and lithium chloride (LiCl, ≥ 95%) were purchased from Sigma-Aldrich. Di-sodium hydrogen phosphate (Na_2HPO_4, anhydrous) and potassium dihydrogen phosphate (KH_2PO_4, anhydrous) purchased from Sigma-Aldrich were used to prepare pH 7 buffered solutions, which provided the aqueous phase in our aqueous|organic biphasic system. The final concentrations of phosphate salts were 60 mM Na_2HPO_4 and 20 mM KH_2PO_4 to achieve pH 7. Lithium tetrakis(pentafluorophenyl)borate diethyletherate (LiTB) was received from Boulder Scientific Company. The organic electrolyte salt of bis(triphenylphosphoranylidene)ammonium tetrakis(pentafluorophenyl)borate (BATB) was prepared by metathesis of equimolar solutions of BACl and LiTB in a methanol-water (2:1 v/v) mixture. The resulting precipitates were filtered, washed and recrystallised from acetone. Cytochrome *c* from bovine heart (Cyt *c*, ≥ 95%, 12.327 kDa) was purchased from Sigma-Aldrich in its oxidised form and used without further purification. Purity and homogeneity of the protein samples have been determined by SDS-PAGE and gel-filtration, respectively.

S1.2 Electrochemical experiments at the electrified aqueous|organic interface. Electrochemical measurements at the aqueous|organic interface formed between an aqueous phosphate buffer solution and organic TFT solution, containing 5 mM BATB organic electrolyte, were performed using a four-electrode electrochemical cell with an interfacial area of 1.53 cm^2. A theoretical background to such experiments at an ITIES can be found in several articles and book chapters.[1–4] All the electrochemical measurements were carried out with a WaveDriver 20 bipotentiostat from Pine Research Instrumentation, Inc., and controlled using AfterMath software version 1.4. The composition of the four-electrode electrochemical cells used are described in Scheme 1 of the main text.

The applied potential (E) in the four-electrode cell used to obtain cyclic voltammograms at the electrified water|TFT interface is defined as the potential difference established between the Ag/AgCl (KCl gel) reference electrode in the aqueous phase and that

in the organic reference solution. The applied potential (E) encompasses the interfacial Galvani potential difference ($\Delta_o^w\phi$). The latter is defined as $\Delta_o^w\phi = (\phi^w - \phi^o)$, where ϕ^w and ϕ^o are the inner Galvani potentials of the aqueous and organic phases, respectively. Additionally, the applied potential (E) is determined by the nature of the reference electrodes used. These contributions to the applied potential (E) are defined here as $\Delta E_{\text{ref.}}$. The calibration of the cyclic voltammograms and differential capacitance measurements obtained at the electrified water|TFT interface to the Galvani potential scale was performed following the relationship $E = \Delta_o^w\phi + \Delta E_{\text{ref}}$. The critical value of ΔE_{ref} was determined using the electrochemical half-wave ion transfer response of TEA^+ ($E_{1/2,TEA^+}^{w\rightarrow TFT}$) and the standard ion transfer potential of TEA^+ from the aqueous to TFT phase (known to be $\Delta_o^w\phi_{tr.,TEA^+}^{\Theta,w\rightarrow TFT} = 0.149$ V),[5] as outlined in detail in our previous work.[6]

Cyclic voltammograms obtained with TEA^+ in the presence of Cyt *c* and various molar concentrations of GdmCl or urea in the aqueous phase are shown in Fig. S1. Upon increasing the concentration of GdmCl in the aqueous phase, while the chaotropic Gdm^+ cation concentration increases (from 2 to 8 M), so too does the chloride anion (Cl^-) concentration. Unlike an Ag/AgCl (KCl gel) reference electrode where the KCl gel contains ca. 3 M Cl^-, a *pseudo*-reference Ag/AgCl electrode will equilibrate with the chloride anions in the aqueous phase leading to the polarisable potential window shifting negatively. Thus, for concentrations ≥3 M (so 4 M and 6 M GdmCl in Fig. S1a), the Cl^- equilibrium is established and invariant, and the polarisable potential window stops shifting negatively (as seen in Fig. S1a comparing $E_{1/2,TEA^+}^{w\rightarrow TFT}$ for 2 M GdmCl to that for 4 M and 6 M GdmCl).

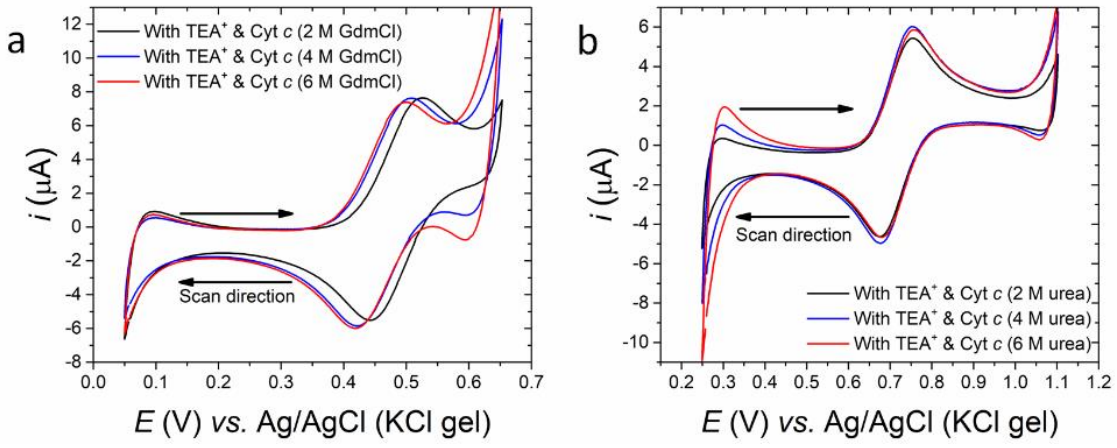

Fig. S1. Comparison of cyclic voltammograms with Cyt *c* and 44 μM tetraethylammonium cations (TEA^+) in the presence of (a) 2, 4 or 6 M GdmCl and (b) 2, 4 or 6 M urea in the aqueous phase. The configuration of the four-electrode electrochemical cell used is described in main

text Scheme 1 with the exception that no decamethylferrocene (DcMFc) was added to the organic phase in this experiment. The scan rate was 20 $mV \cdot s^{-1}$. All electrochemical measurements were carried out under ambient, aerobic conditions.

Previously, Peljo *et al*. noted that the presence of urea in the aqueous phase affected the energetics of ion transfer of tetraalkylammonium cations and dyes by modifying their ion solvation.[7] While this effect was significant for a series of phenothiazine dyes studied (with negative shifts of their standard ion potentials of between 50 and 100 mV at the water|TFT interface), the effect was relatively minor (shifts of up to ~10 mV) for a series of tetraalkyammonium cations. Here, we demonstrate that with increasing concentrations from 2 M to 8 M of urea in the aqueous phase, $E_{1/2,\mathrm{TEA}^+}^{\mathrm{w}\rightarrow\mathrm{TFT}}$ remains constant.

AC voltammetry was performed in a four-electrode electrochemical cell. Differential capacitance was calculated from the interfacial admittance recorded using an Autolab FRA32M module in combination with the Autolab PGSTAT204 at a frequency of 5 Hz (unless noted otherwise) and root mean square (RMS) amplitude of 5 mV. The scan direction was from negative towards more positive potentials, from ca. –0.3 to +0.55 V. Unlike impedance spectroscopy, where a wide range of frequencies are tested at a constant potential, differential capacitance measurements are performed at a constant frequency and $\Delta_{\mathrm{o}}^{\mathrm{w}}\phi$ is varied. Furthermore, the range of frequencies permitted at an electrified aqueous|organic interface to carry out differential capacitance measurements is limited typically from 1 to 80 Hz, as recently clarified by Suarez-Herrera *et al.*[1]

S1.3 UV/vis spectroscopy. UV/vis absorbance measurements were performed using the parallel beam configuration. The light source, DH-2000-BAL deuterium–halogen (Ocean Optics), was directed through the quartz cuvette with the use of an UVFS coated plano convex lens (Thorlabs) and an iris diaphragm (Thorlabs). After transmission through the cuvette, the light source was focused by a second UVFS coated plano convex lens (Thorlabs) to a Maya 2000 Pro Spectrometer (Ocean Optics).

S1.4 Raman spectroscopy. Raman spectroscopic measurements were performed using a LabRAM HR Evolution Raman Confocal Microscope (Horiba, France) with LabSpec 6 software. Measurements were performed with a 532 nm excitation line source and 50 µL of 10 µM Cyt *c* and chaotrope solutions of given concentrations. Calibration was performed with a silicon standard (520.07 cm^{-1}).

S2. Supplementary electrochemical and spectroscopic figures

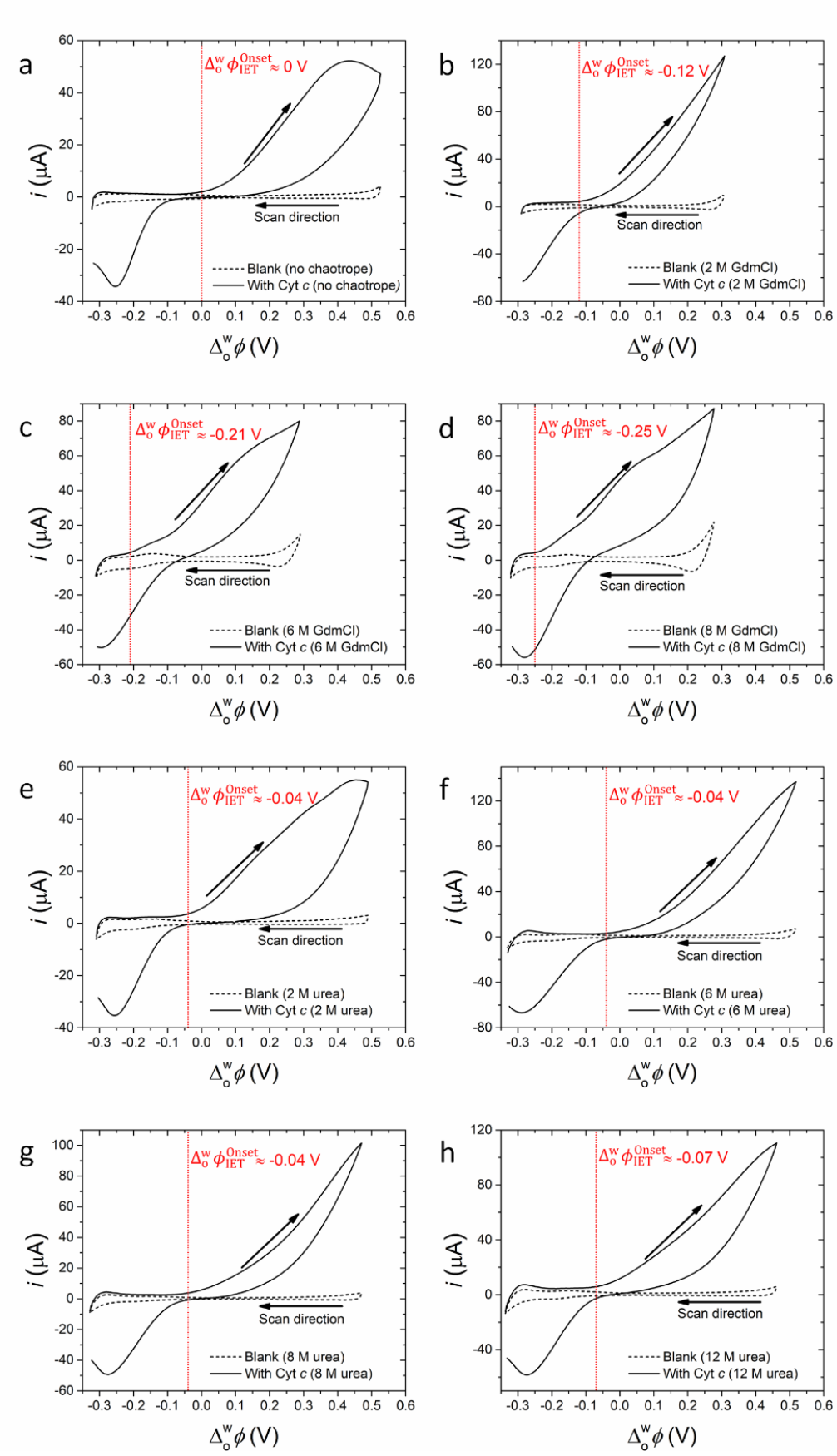

Fig. S2. Comparison of cyclic voltammograms in the absence and presence of Cyt *c* (a) without a chaotrope in the aqueous phase and in the presence of (b) 2 M GdmCl, (c) 6 M GdmCl, (d) 8 M GdmCl, (e) 2 M urea, (f), 6 M urea (g) 8 M urea and (h) 12 M urea. The onset potential ($\Delta_o^w\phi_{IET}^{Onset}$) was determined as the value of $\Delta_o^w\phi$ where the current deviates compared to the blank voltammogram. The configuration of the four-electrode electrochemical cell used is described in Scheme 1 and the scan rate was 20 mV·s^{-1}. All electrochemical measurements were carried out under ambient, aerobic conditions.

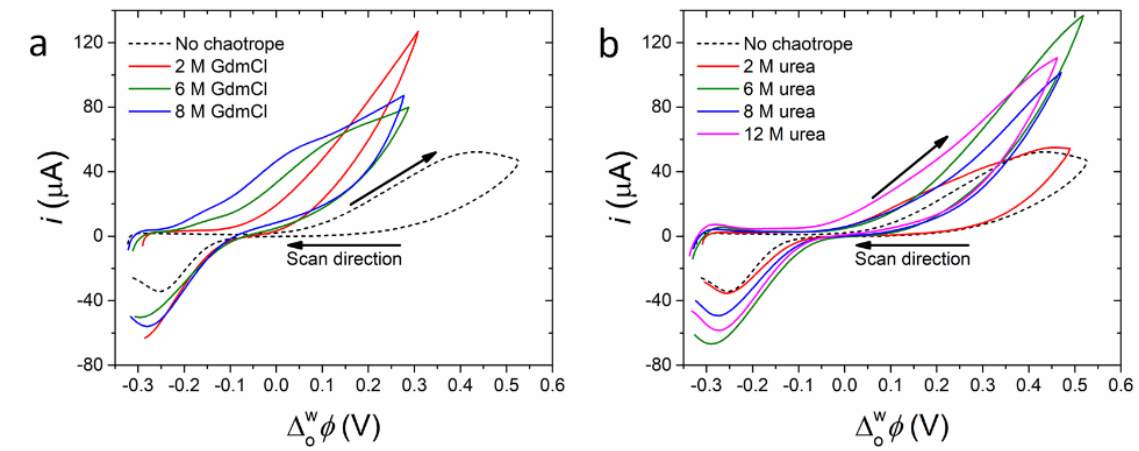

Fig. S3. Comparison of cyclic voltammograms in the presence of Cyt *c* (a) without a chaotrope in the aqueous phase and in the presence of 2, 6 and 8 M GdmCl and (b) without a chaotrope and in the presence of 2, 6, 8 and 12 M urea. The configuration of the four-electrode electrochemical cell used is described in Scheme 1 and the scan rate was 20 mV·s^{-1}. All electrochemical measurements were carried out under ambient, aerobic conditions.

Studying the relationship between current and scan rate in the presence and absence of a chaotrope would provide insights into changes of the heterogeneous electron transfer rate constants and possible mass transport limitations by diffusion of reactive species. However, as seen in Fig. 1a and Fig. S3, some of the voltammetric signals did not present well-defined peak currents despite the relatively slow scan rates used during the voltammetric characterisation (20 mV s^{-1}). Furthermore, experiments at higher scan rates (>100 mV s^{-1}) are unsuitable for performing electrochemistry at an electrified aqueous|organic interface due to an *iR* drop that is mainly attributed to the organic solvent polarisation. Thus, future work involving Cyt *c* and chaotropes will be performed using micro-interfaces to eliminate any possible ohmic drop or mass transport limitations.

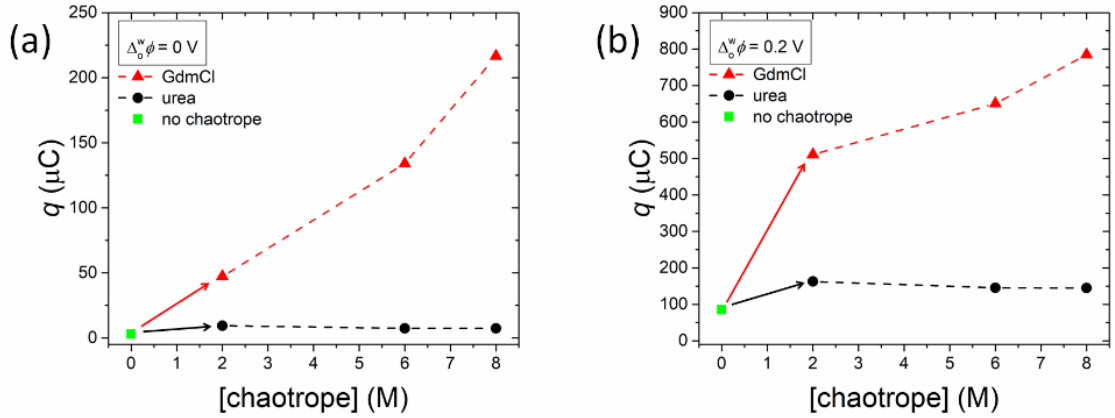

Fig. S4. Charge transfer (q) attributed to ROS production by Cyt *c* in the absence and presence of increasing concentrations of the aqueous chaotropes GdmCl and urea at (a) $\Delta_o^w\phi$ = 0 V and (b) $\Delta_o^w\phi$ = 0.2 V, respectively. The charge transfer in each case was determined from the cyclic voltammograms shown in Fig. 1a and Fig. S3. The integration was performed across the potential range of –0.25 to 0.0 V in (a) and –0.25 to 0.2 V in (b).

At both 0.0 and 0.2V, a near linear trend between increasing charge and increasing GdmCl concentration was detected (Fig. S4). For example, at 0.0 V, the charge rose 40- and 200-fold in the presence of 2 and 8 M GdmCl, respectively, above the charge recorded with no chaotrope present (Fig. S4a). On the other hand, in the presence of urea, the charge transfer at 0.0 V was constant and comparable to that recorded with no chaotrope present (Fig. S4a). Nevertheless, at 0.2 V (Fig. S4b), the charge transfer rose slightly in comparison to that with no chaotrope present to a constant value independent of urea concentration. This straightforward analysis suggests that promotion of ROS production (by IET from DcMFc to O_2 electrocatalysed by adsorbed Cyt *c*) is dramatically improved with GdmCl compared to urea. As discussed in detail in the main text, this is due to physicochemical changes to the water|TFT interface and conformational changes to the adsorbed Cyt *c* in the presence of GdmCl, which work in tandem to increase the probability of DcMFc and O_2 reaching the heme active site.

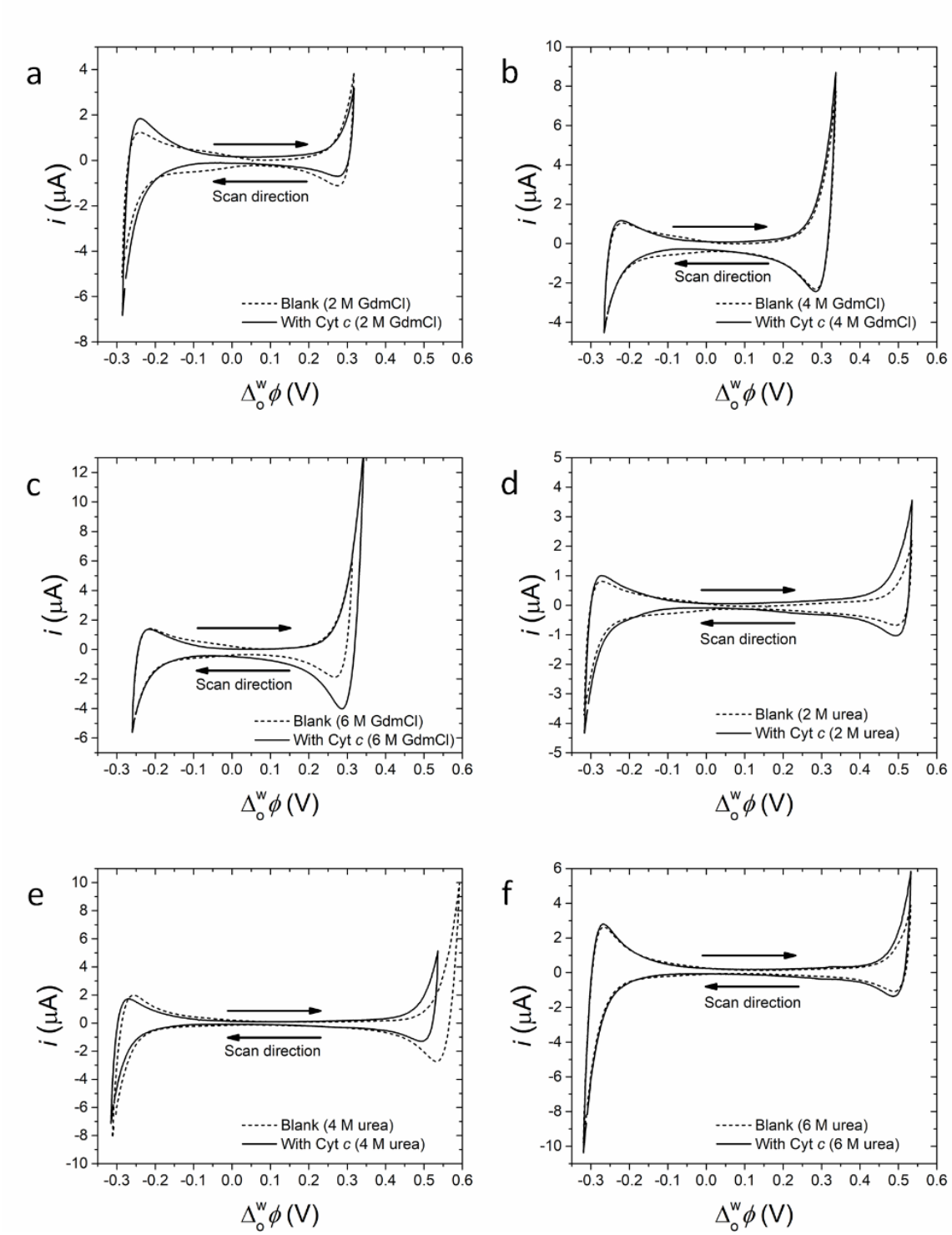

Fig. S5. Control experiments with no DcMFc added to the organic phase comparing cyclic voltammograms with Cyt *c* in the presence of (a) 2 M GdmCl, (b) 4 M GdmCl (c) 6 M GdmCl, (d) 2 M urea, (e) 4 M urea and (f) 6 M urea in the aqueous phase. The configuration of the four-electrode electrochemical cell used is described in Scheme 1 with the exception that no DcMFc was added to the organic phase. The scan rate was 20 $mV \cdot s^{-1}$. All electrochemical measurements were carried out under ambient, aerobic conditions.

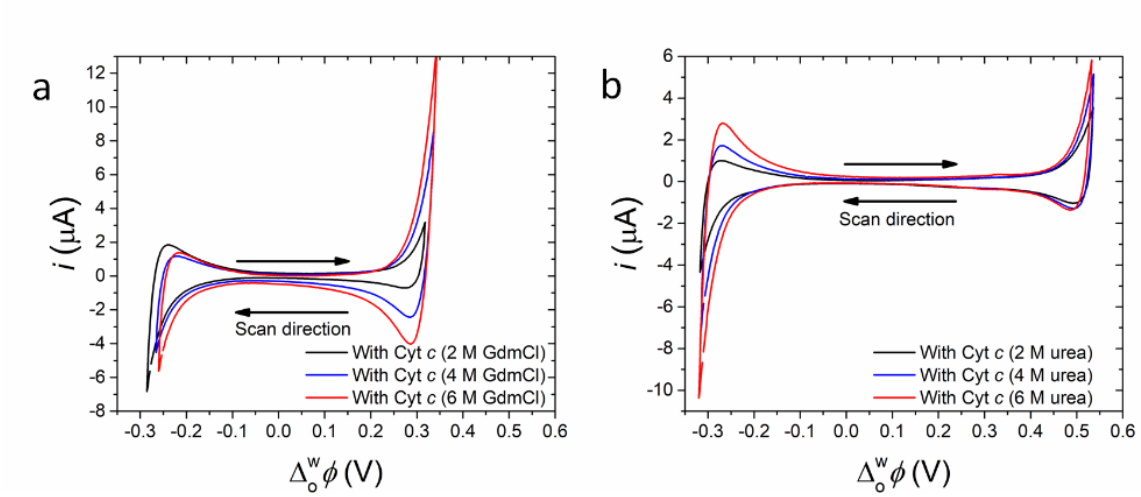

Fig. S6. Control experiments with no DcMFc added to the organic phase, comparing cyclic voltammograms with Cyt *c* in the presence of (a) 2, 4 and 6 M GdmCl and (b) 2, 4 and 6 M urea in the aqueous phase. The configuration of the four-electrode electrochemical cell used is described in Scheme 1 with the exception that no DcMFc was added to the organic phase. The scan rate used was 20 $mV \cdot s^{-1}$. All electrochemical measurements were carried out under ambient, aerobic conditions.

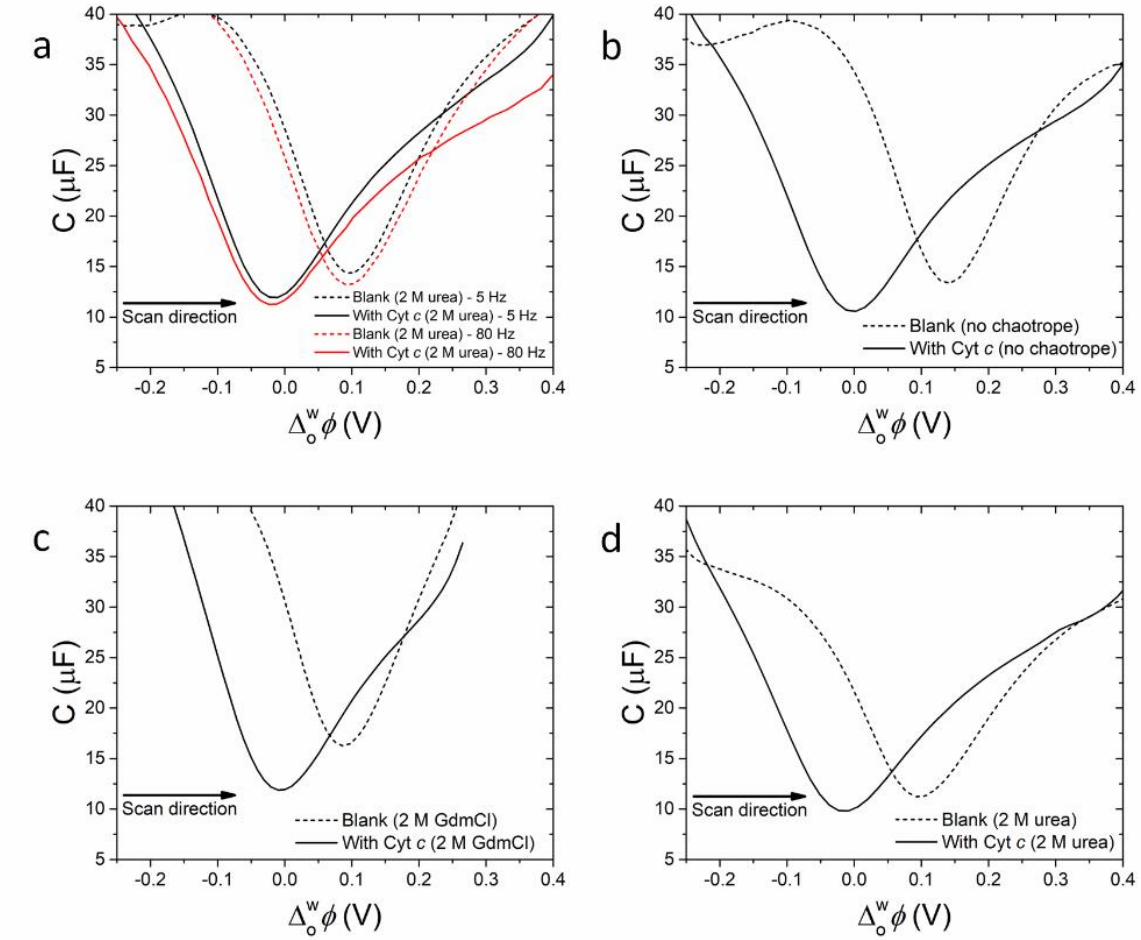

Fig. S7. (a) Comparing the influence of the applied AC frequency (5 *versus* 80 Hz) on differential capacitance measurements in the presence of urea, with and without Cyt *c*. (b)-(d) Differential capacitance measurements in the absence and presence of Cyt *c*, (b) without a

chaotrope in the aqueous phase and in the presence of (c) 2 M GdmCl and (d) 2 M urea. The configuration of the four-electrode electrochemical cell used is described in Scheme 1 and all capacitances were measured using an AC frequency of 5 Hz, unless stated otherwise. All electrochemical measurements were carried out under ambient, aerobic conditions.

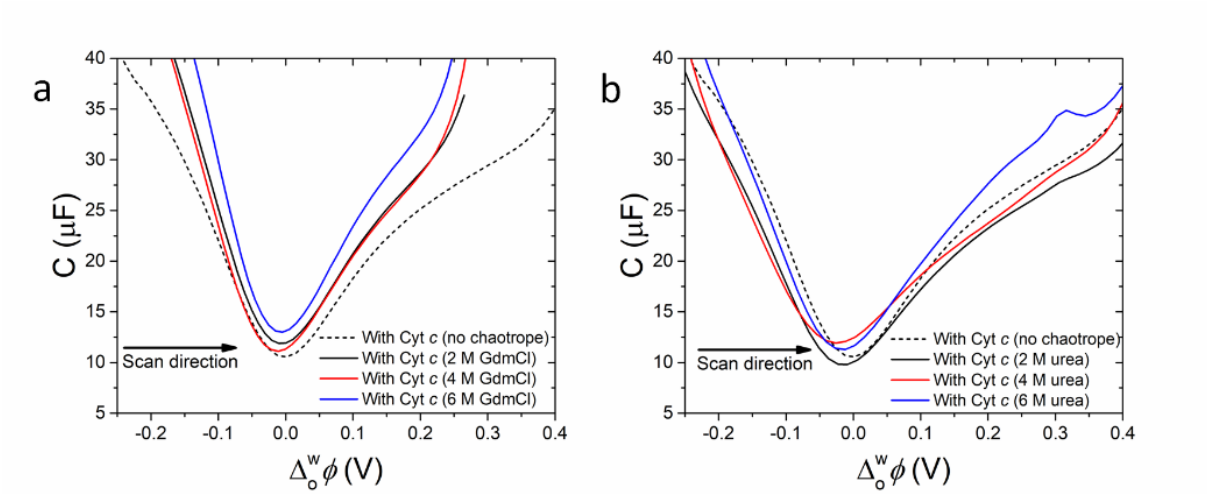

Fig. S8. Comparison of differential capacitance measurements in the presence of Cyt *c* (a) without a chaotrope in the aqueous phase and in the presence of 2, 4 and 6 M GdmCl and (b) without a chaotrope and in the presence of 2, 4 and 6 M urea. The configuration of the four-electrode electrochemical cell used is described in Scheme 1 and all capacitances were measured using an AC frequency of 5 Hz, unless stated otherwise. All electrochemical measurements were carried out under ambient, aerobic conditions.

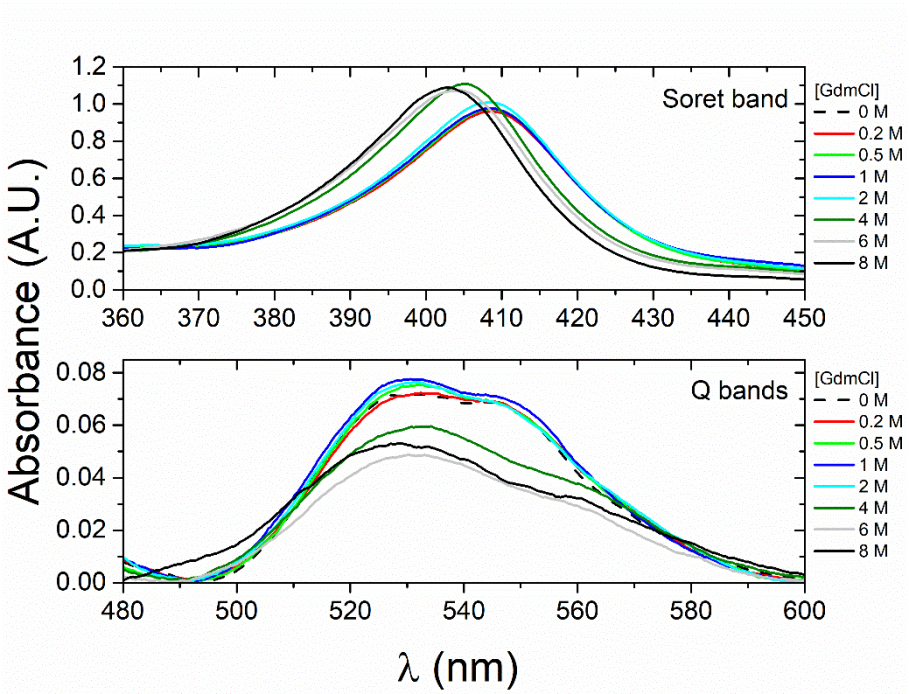

Fig. S9. UV/vis absorbance spectra of 10 μM Cyt *c* in phosphate buffer at pH 7 with increasing concentrations of GdmCl added to the aqueous phase. For clarity, the Soret and Q bands are plotted individually. During these experiments, no cloudiness was observed in the aqueous phase, even up to a concentration of 8 M GdmCl in the aqueous phase. Furthermore, cyclic voltammograms recorded in the presence of 8 M GdmCl were stable, as shown in Fig. S5.

Thus, the high chaotrope concentrations did not influence our UV/vis absorbance measurements. Furthermore, the same observations (no cloudiness in the aqueous phase and stable cyclic voltammograms) were obtained for all concentrations of urea investigated.

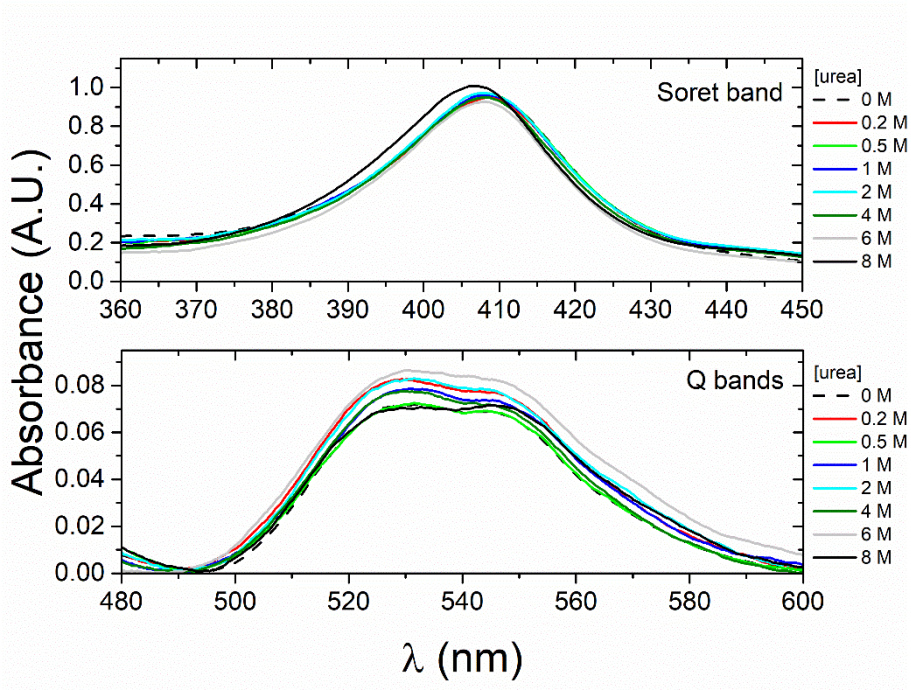

Fig. S10. UV/vis absorbance spectra of 10 μM Cyt *c* in phosphate buffer at pH 7 with increasing concentrations of urea added to the aqueous phase. For clarity, the Soret and Q bands are plotted individually.

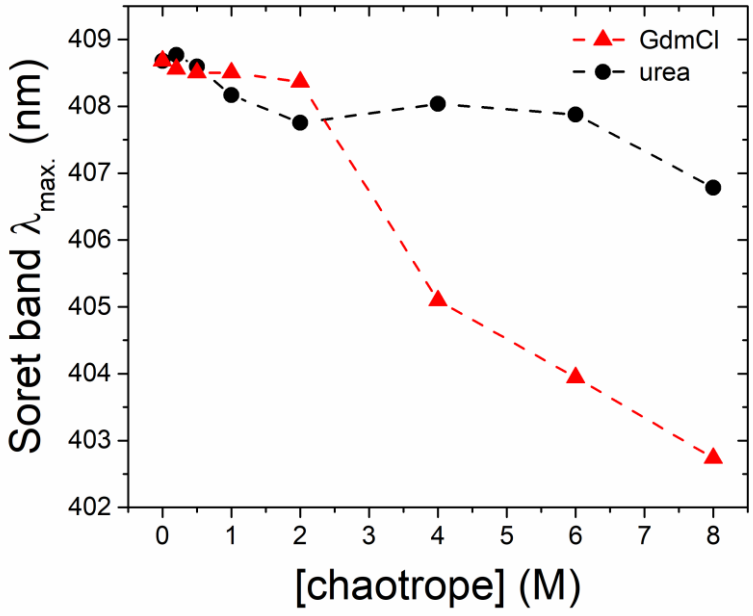

Fig. S11. Shifts of the Cyt *c* Soret band maximum absorbance ($\lambda_{max.}$ / nm) with increasing chaotrope concentration in the aqueous phase. The UV/vis spectra for GdmCl and urea are shown in Figs. S9 and S10.

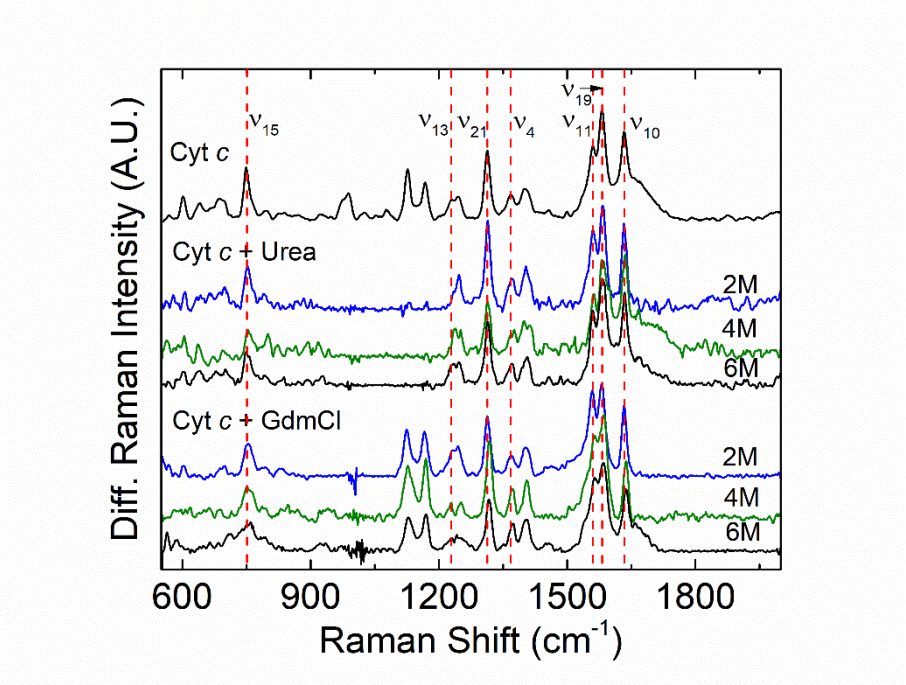

Fig. S12. Shifts of the Raman intensity and frequency of 10 μM Cyt *c* in phosphate buffer at pH 7 with increasing concentrations of urea and GdmCl added to the aqueous phase.

Table S1. Observed in-plane skeletal frequencies of ferric Cyt *c* in the presence of chaotropes (data read from Fig. S12).

Skeletal Frequencies	Phosphate buffer	GdmCl 2 M (6 M)	Urea 2 M (6 M)
ν_{15} *(pyr breathing)*	749	754 (undef)	752 (748)
ν_{13} $\delta(C_mH)$	1229	1230 (undef)	1234 (1234)
ν_{21} $\delta(C_mH)$	1313	1313 (1318)	1314 (1314)
ν_4 *(pyr half-ring)*$_{sym}$	1368	1369 (1374)	1371 (1370)
ν_{11} $(C_\beta C_\beta)$	1560	1558 (1564)	1560 (1559)
ν_{19} $(C_\alpha C_m)_{assym}$	1581	1581 (1585)	1583 (1582)
ν_{10} $(C_\alpha C_m)_{assym}$	1633	1633 (1637)	1633 (1635)

Frequency shifts seen for skeletal modes are mainly due to a combination of core-expansion and more Fe–porphyrin backbonding in Cyt *c*. The high-frequency skeletal modes, υ_{10}, υ_{11}, and υ_{19}, are sensitive to both core size expansion and backbonding, whereas changes in υ_4 is mostly due to backbonding.[8] Note that υ_{15} (pyrrole breathing) and υ_{13} are drastically altered and weakened with 6 M GdmCl, signalling a major heme exposure.

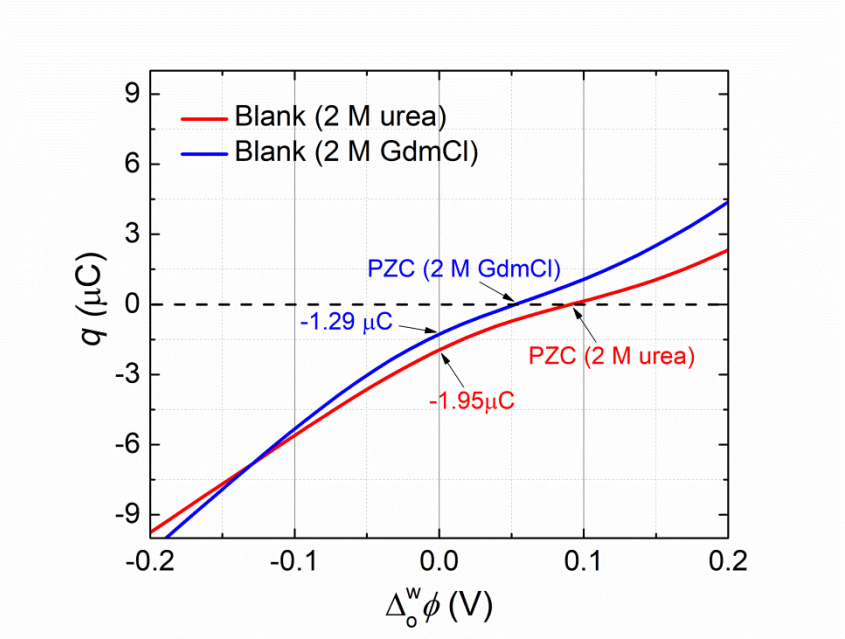

Fig. S13. Plots of the interfacial charge (q) *vs.* interfacial Galvani potential difference ($\Delta_o^w\phi$) estimated from the integration of the differential capacitance data presented in main text Fig. 1c with 2 M of either urea or GdmCl in the aqueous phase.

The potential of zero charge (PZC) is the potential that marks the change of the net charge at the boundaries of the aqueous phase. From the PZC towards more positive potentials, the aqueous phase is charged positively, and the concentration of aqueous cations near the interface is greater than the bulk solution. On the other hand, from the PZC towards less positive potentials, the aqueous phase is charged negatively, and the concentration of aqueous anions near the interface is greater than the bulk aqueous phase. Note that at 0.0V the aqueous|organic interface is considered negatively charged in the presence of either 2M urea (–1.95 μC) or 2 M GdmCl (–1.29 μC) in the aqueous phase. From this data, to simulate the charging process at 0.0 V, we multiplied the bulk aqueous and organic electrolyte concentrations by a factor of 1.95 for urea and 1.29 for GdmCl to reflect the measured interfacial concentrations (Fig. S12). Thus, at 0.0 V, $H_2PO_4^-$ and HPO_4^{2-} anions balance the positive charge of BA^+.

S3. Molecular Dynamics Simulations and Analyses

S3.1 Preparation of the models. A 1.5 Å resolution crystal structure of ferri (oxidised, Fe^{3+} heme) Cyt *c* from bovine heart (PDB code 2B4Z)[9] was used as the starting model for the protein. Hydrogen atoms were placed using the Schrödinger Maestro[10] package.[11] The heme (Fe^{3+}) of native state Cyt *c* is axially coordinated to the His18 and Met80 residues.[12] In order to closely mimic the experimental observation that the axial Fe(III)–(S)Met coordination in Cyt *c* is lost in the presence of 2 M denaturing agent guanidinium chloride (GdmCl), we broke the Met80-heme bond and reparametrized accordingly, to create the models in GdmCl, as reported in a previous study in the presence of 1.5 M GdmCl.[8] We kept the Met80-heme bond intact in the presence of 2 M urea. We also performed control simulations of the experimentally non-observed state with the bond intact in Cyt *c* in the presence of 2M GdmCl.

A rectangular box with edge lengths 10 nm x 10 nm x 40 nm containing solvent molecules of water and α,α,α-trifluorotoluene (TFT) was built to form the aqueous|organic interface (20 nm depth in each phase) with full periodic boundary conditions applied in all three directions. To model the migration of the chaotropes to the interface and interaction with protein within a reasonable computational time, we scaled the experimental ion concentrations to mimic high local concentrations of ions at the interface. In the presence of urea, the charged ions were included at 1.95 times their bulk concentrations, while in presence of GdmCl, the charged ions were added at 1.29 times their bulk concentrations (see Fig. S13, Section S2 above). To delineate the specific effect of the interface on conformational shifts and partial unfolding of Cyt *c*, we performed additional simulations in the presence of 2 M urea and GdmCl in pure water retaining the experimental ion concentration in water, but without the TFT phase and its associated ions.

S3.2 Molecular simulation details. All molecular dynamics (MD) simulations were performed with the Gromacs 2018.4 package using the CHARMM36m forcefield[13] and the CHARMM-modified TIP3P[14] water model. The forcefield parameters for the oxidised state of the heme were obtained from Supplementary ref. [15]. We applied a harmonic constraint with force constant of 1,000 kJ/mol/nm^2 on the protein centre of mass to slowly pull the Cyt *c* towards the interface. Covalent bonds to hydrogen in protein and water were constrained using the LINCS[16] and SETTLE[17] algorithms, respectively. This allowed the leapfrog integrator[18] to be used with a time step of 2 fs, and coordinates were saved every 20 ps. Long-range electrostatics were treated by the Particle Mesh Ewald (PME) method.[19] All systems were minimised for 10,000 steps and equilibrated and thermalised to 300 K during 1 ns of constant

volume dynamics followed by 1 ns at constant pressure of 1 bar with a time constant of 5 ps using the Berendsen barostat.[20] All molecules were coupled separately in groups to an external heat bath with a coupling time constant of 1 ps using the Berendsen method.[20] The production runs were carried out for 0.5 μs for each system in the constant pressure and temperature NPT ensemble. The pure aqueous phase simulations were performed using the same protocol.

S3.3 MD data analysis. All analyses (main text Fig. 2 and Figs. S13 – S20 below) of density profiles, root mean square deviation (RMSD), root mean square fluctuation (RMSF), interaction energies and dielectric constants were performed using Gromacs tools. The fraction of native contacts, tilt angle and secondary structure of the protein were mapped using Python scripts. The MD trajectories were visualised using Visual Molecular Dynamics (VMD).[21]

The solvent-accessible surface area (SASA) of the part of Cyt *c* only exposed to water but not to the interface, was computed by using the "restrict" function in VMD using Tcl scripts. In addition, we computed the SASA of only the hydrophobic residues in Cyt *c* exposed to both the water phase and the aqueous|organic interface (Figs. S16 and S19e, f).

The fraction of native contacts Q (Figs. S18b, S20f) was calculated using the definition from Best, Hummer and Eaton,[22] implemented in the MDTraj[23] python library, using the equation:

$$Q = \frac{1}{N}\sum_{i,j}\frac{1}{1+\exp\left[\beta\left(r_{ij}(t)-\lambda r_{ij}^{0}\right)\right]} \quad \text{(S1)}$$

where *N* is the set of all pairs of heavy atoms *(i, j)*, and heavy atoms *i* and *j* are in contact if the distance between them is less than 5 Å and they are separated by at least 3 residues. $r_{ij}(t)$ is the distance between *i* and *j* in the structure sampled at time t and r_{ij}^{0} is the distance in the starting structure at time 0. β is a smoothening parameter taken to be 5 $Å^{-1}$ and λ is a factor that describes fluctuations when the contact is formed, taken to be 1.8 for the all-atom model. For more details on the method and choice of parameter values, please see Supplementary ref. [22].

S3.4 Supplementary analysis. We provide further details of additional analyses from our MD simulations here to support the main findings. All input and output files of simulations are available on request from corresponding author damien.thompson@ul.ie.

From the computed density profiles (main text Fig. 2a, b), a dip in the water density distribution close to the interface identifies the position of Cyt *c* in the presence of 2 M urea (Urea-bonded) and 2 M GdmCl (GdmCl-broken), with Cyt *c* sitting ~3 Å closer to the interface with urea compared to GdmCl. The smaller concentration of Gdm^{+} at the interface will expedite

the interfacial water|TFT mixing enhancing the hydrophobicity of the interface (Fig. 2b), as reflected by a decrease in the predicted dielectric constant from ~40 in the presence of urea to~30 in the presence of GdmCl (Fig. S18a). On the other hand, the higher concentration of urea at the interface would be expected to partially impede access of TFT to the water phase, as observed from the slight shift in position corresponding to the interfacial TFT when urea is present (Fig. 2a). The opening of the heme pocket coupled with its interface-ordered orientation is quite evident for both chaotropes (Fig. 2c) and is likely to promote interfacial electron transfer (IET, Fig. 1a). The interface-facilitated normal orientation of Cyt *c* is also evident in the system devoid of chaotropes (at positive biasing potential; shown as "No chaotropes" in Fig. S14a), but in the presence of GdmCl with the Met80–heme bond intact (GdmCl-bonded in Fig. S14a), no preferred orientation of Cyt *c* at the interface was observed (Fig. S14a).

The simulations indicate that this pre-organisation of the protein for IET follows different mechanisms, as deduced from the computed Cyt *c* residue-wise fluctuations (RMSF Dev.) with respect to the initial structure as reference (Fig. 2d). The comparative RMSF Dev. plots (Fig. S14b) for all interface systems in this study reveal that with the Met80 and heme bonded in Cyt *c*, in the presence of both urea and GdmCl, residue ranges 40–57 constituting the Ω loop domain[24,25] show increased loop dynamics, which may regulate Cyt *c* heme pocket opening under native conditions (see main text, and also data for Urea-bonded and GdmCl-broken models in Fig. S14b). However, for the unpopulated, artificial GdmCl-bonded state, in addition to the Ω loop, the loop-A is seen to undergo increased fluctuation. The computed structures from this control simulation suggests that the concerted dynamicity of these two loop domains would hinder ordered alignment of Cyt *c* at the interface (Fig. S14a). This increased fluctuation in the Ω loop is minor when the Met80–heme bond is broken in the presence of GdmCl (GdmCl-broken in Fig. S14b), but dynamic fluctuations in loops surrounding the heme, loop-A[26] (spanning residues 20–30) and loop-D[27] (spanning residues 76–82) are dominant (absent in Urea-bonded), and guide opening of the heme pocket in Cyt *c* (Fig. S14b). On the other hand, in the complete absence of denaturing agents ("No chaotropes" in Fig. S14b), only loop-A shows increased fluctuation and the interface–ordered orientation of Cyt *c* (Fig. S14a) could be solely attributed to the high local concentration of TB^- to anchor the protein surface Lys residues at positive biasing potential, which is not the case in presence of chaotropes (Figs. 2a, b).

Thus, in the presence of GdmCl, the dissociation of the heme Fe(III)–(S)Met80 bond promotes opening of the pocket by immediately exposing the loops surrounding the heme to

the interface, as identified from the slightly larger structural RMSD in GdmCl-broken at the start of simulation in Fig. S14c. With bonded heme Fe(III)–(S)Met80, in the presence of both urea (Urea-bonded) and GdmCl (GdmCl-bonded), the region corresponding to the Ω loop domain flips open halfway through the simulation exposing the heme pocket to the interface, triggering structural rearrangements during the remaining 0.25 μs of dynamics (Fig. S14c), with large conformational mobility of Cyt *c* residues in the Ω loop (Fig. S14d). The loop domains responsible for these distinct mechanisms of opening of the heme pocket in presence of both chaotropes is represented on the Cyt *c* structure in the inset of Fig. S14d.

To identify the interactions driving these conformational shifts and rearrangements, we computed interaction energies (Coulombic/electrostatic and van der Waals energies) between Cyt *c*, and solvent TFT, electrochemical ions, and chaotropes (Figs. S15 and S19c, d). The stronger interaction with GdmCl (for both GdmCl-broken and GdmCl-bonded) than with urea (Figs. S15a, b and S19c) reflects the stronger build-up of GdmCl on the protein (Figs. 2a, b and S19a). The interaction energies normalised per molecule of TFT, and ionic species, (Figs. 15c, d and S19d) show that TB^- interactions with Cyt *c* are non-specific and weak due to a low local concentration of TB^- at the interface. In the presence of urea, the overall openness, or solvent accessible surface area, SASA of Cyt *c* increases over time, especially after 0.25 μs (Fig. S16a) where the greater flexibility of the Ω loop domain is observed (Fig. S15a). GdmCl (Figs. S16b and S19f) does not improve the overall SASA of Cyt *c* as much as when urea (Fig. S16a) is present, and reduced surface exposure to water (and other small polar or charged environmental molecules) is observed. This shielding from water is also evident when restricted to the hydrophobic residues only of Cyt *c*; the increase in SASA at the interface side after ~0.35 μs of dynamics (Figs. S16d and S19e) indicates the tendency of Cyt *c* to slowly navigate towards the interface, sitting more distant from the interface in the presence of GdmCl than in the presence of urea (see Figs. 2a, b and S19a).

To further map how the heme pocket opening couples with partial unfolding of Cyt *c*, we tracked the evolution of secondary structure (Figs. S17 and S19b) and native contacts (Fig. S18b) as a function of simulation time. We observe that in the presence of both chaotropes, the Cyt *c* presents a more open structure than in their absence, as evident from the faster and larger loss of native contacts (Fig. S18b). Particularly, the opening of the heme pocket for the GdmCl-broken system is reflected by a large drop in native contacts at the beginning of dynamics due to the dissociation of the Met80-Heme bond, which further increases during the second half of dynamics (at ~0.35 μs) as the Ω loop loses its native contacts with other domains in Cyt *c*, with

bend and turn conformations replacing α-helix (Fig. S17b). In the presence of urea, there is an initial decay in contacts, with loss in the α-helical and turn motifs between ~0–0.06 μs (Fig. S17a), followed by another period of faster loss in native contacts between 0.2–0.3 μs, finally evolving with stable contacts until the end of 0.5 μs. Following this observation, we posit that the opening of the heme pocket may facilitate partial unfolding of Cyt *c* in the presence of both denaturing agents. On the other hand, the heme pocket opening due to Ω loop flipping (Fig. S18b) does not ease unfolding of Cyt *c* when the Met80–heme bond is intact in the presence of GdmCl (see Fig. S19b).

We compared the computed relative permittivity (ε_r) of the water phase with and without the chaotropic agents. The data (Fig. S18a) reveals that in the presence of the denaturing agents, there is a significant drop of ε_r (~40 with urea and ~30 with GdmCl, both broken and bonded) compared with ~52 in the absence of chaotropes. This highlights that the presence of denaturing agents disrupts the water structuring, destabilising the Cyt *c* protein structure. The initial large peak of ε_r in the absence of chaotropes signifies the greater effort expended in forming the water|TFT interfacial layer by water dielectric relaxation than in the presence of chaotropes. Thus, a faster dielectric relaxation of water in the presence of GdmCl with no initial peak reflects the ease with which the thick interface is formed (Fig. 2b), compared to the relaxation in the presence of urea, which is consistent with differential interface thicknesses measured in the experiments (main text Fig. 1b-d).

Finally, control simulations without the interface and in the presence of 2 M urea and GdmCl in pure water show less change in Cyt *c* structure over time (see Figs. S20a, b) despite the similar loop dynamics (Fig. S20d) and decay in native contact fractions (Fig. S20f), indicating the importance of interface-ordered organisation of Cyt *c*. Similarly, the radius of gyration (R_{gyr}) in Fig. S20c reveals only marginal loss of compactness of Cyt *c* structure in the presence of chaotropes, but faster dielectric relaxation of water in the presence of GdmCl than in urea (Fig. S20c).

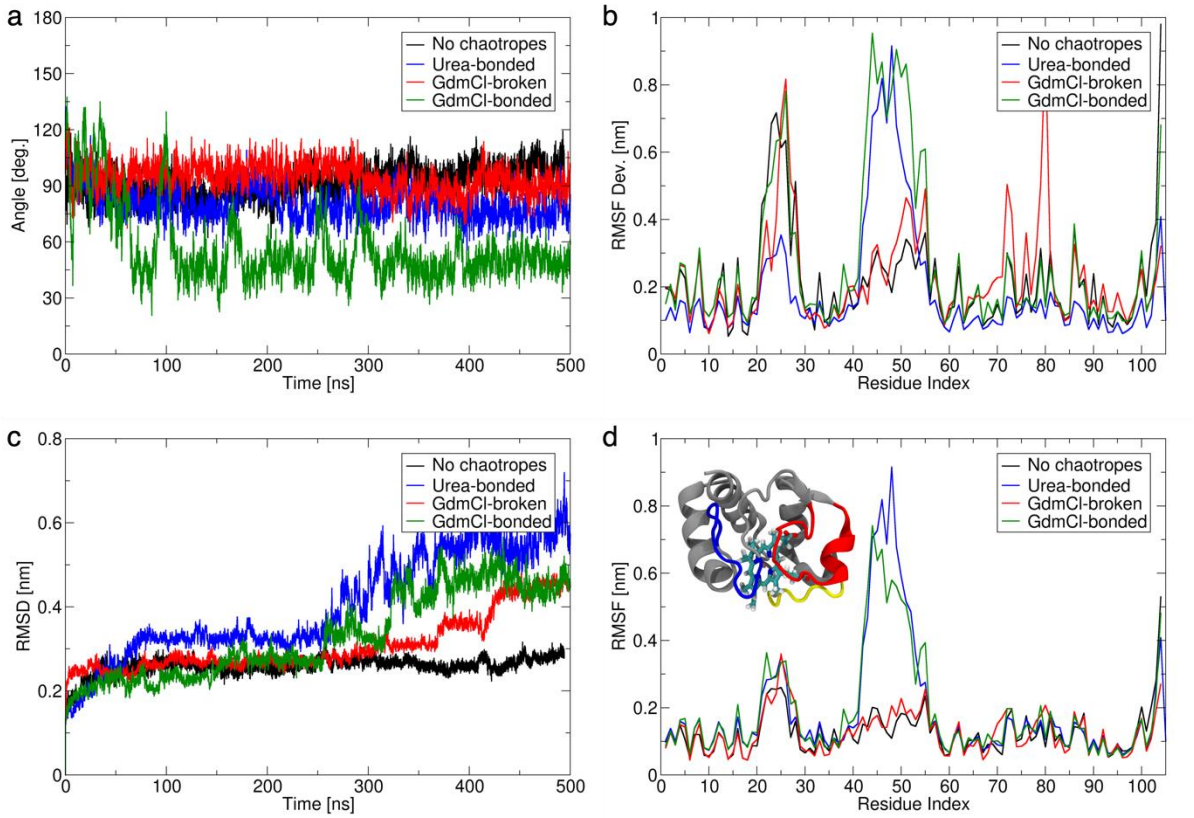

Fig. S14. (a) Simulation timelines showing angles sampled between the heme plane and the interface in the presence of each denaturing agent and in their absence, at positive bias. (b) Per-residue root mean square fluctuation of Cyt *c* amino acid residues (RMSF Dev.) with respect to the starting X-ray structure. (c) Structural deviation of Cyt *c* (RMSD) away from the starting X-ray structure during interactions with chaotropes at the interface. (d) Corresponding root mean square fluctuation (RMSF) of Cyt *c* residues relative to the average MD structure. The inset shows Cyt *c* with the three regions undergoing the largest changes coloured in blue (20-30, loop-A), red (40-57, Ω-loop), and yellow (76-82, loop-D). These regions form three of the four sides of the heme pocket. They are responsible for the different opening/closing mechanisms of the pocket.

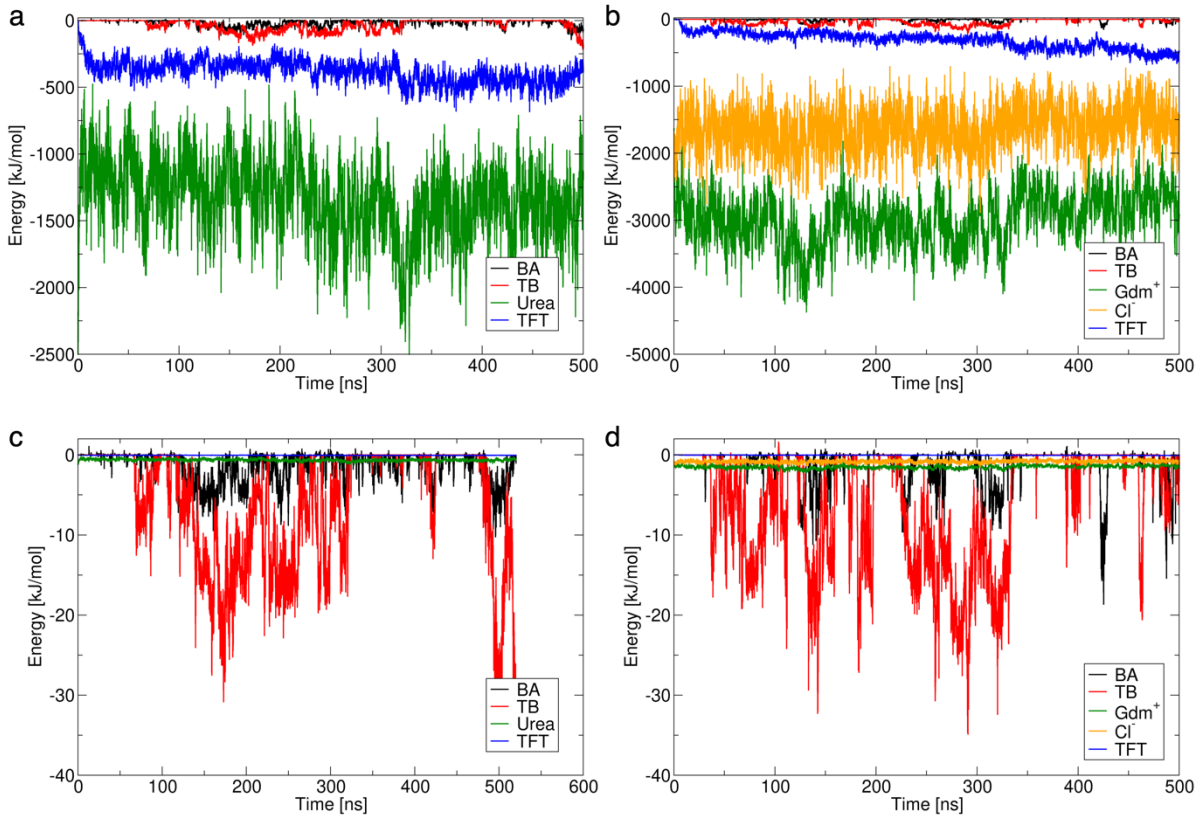

Fig. S15. Short-range interaction energies (electrostatic + van der Waals) between Cyt *c*, and different molecular and ionic species, and solvent TFT in the biphasic systems containing (a) urea and (b) GdmCl as chaotropes. The corresponding interaction energies normalised per molecule of the ionic species and TFT in the presence of (c) urea and (d) GdmCl.

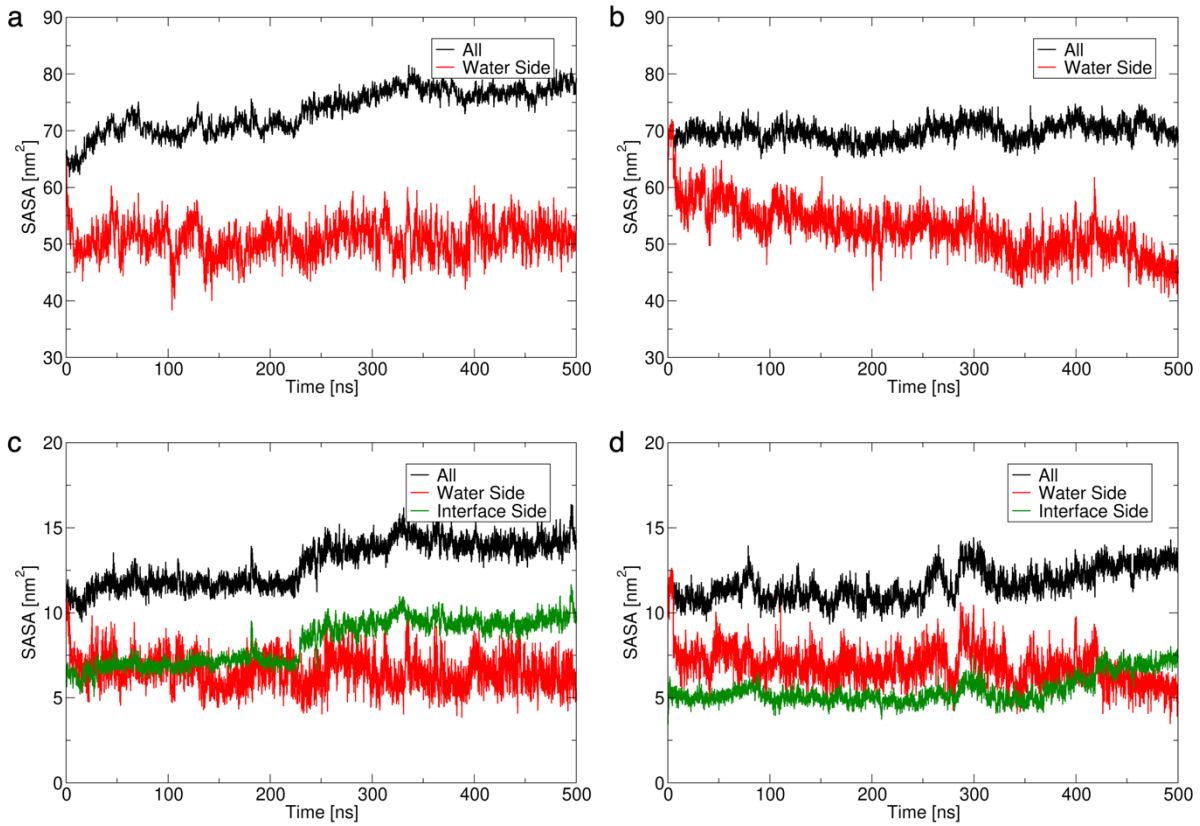

Fig. S16. Time evolution of the solvent-accessible surface area (SASA) of Cyt *c* compared to their exposure to water only in presence of (a) urea and (b) GdmCl. SASA of hydrophobic residues in Cyt *c* compared to their exposure to both water and the interface in presence of (c) urea and (d) GdmCl.

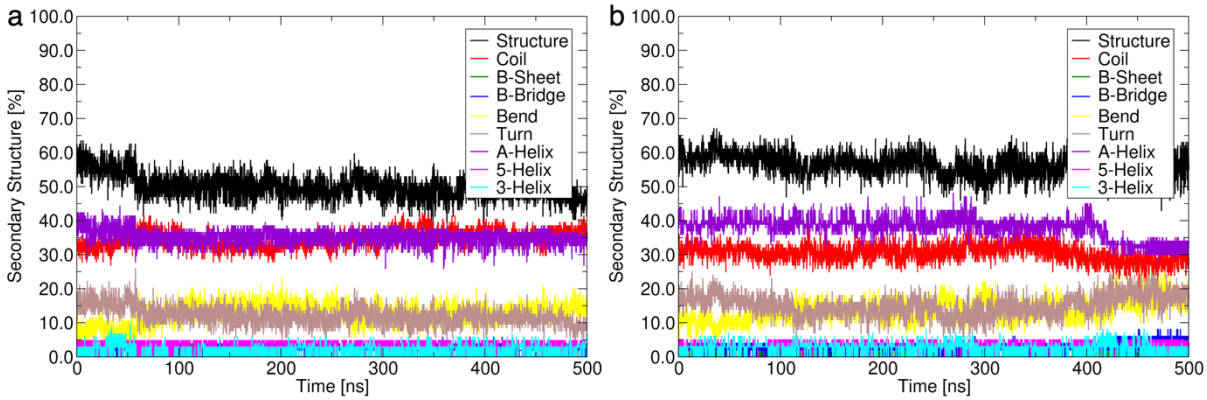

Fig. S17. Evolution of the percent of residues of Cyt *c* populated by different secondary structure elements as a function of simulation time in the presence of (a) urea and (b) GdmCl.

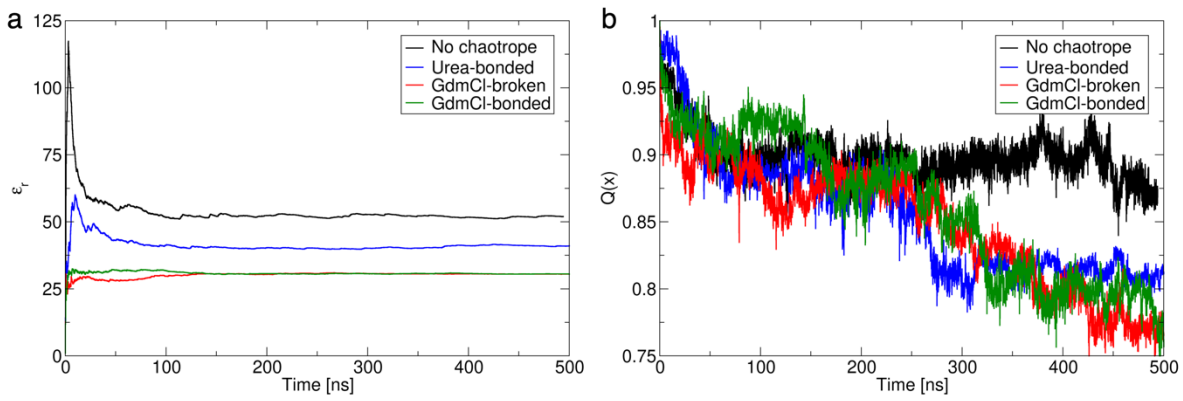

Fig. S18. (a) Time evolution of the relative permittivity (ε_r) of the water phase in MD simulations in the presence of chaotropes, and in control simulations without denaturing agents (black line, None). (b) Fraction of native contacts (Q(X)) of Cyt *c* as a function of simulation time in the presence of chaotropes.

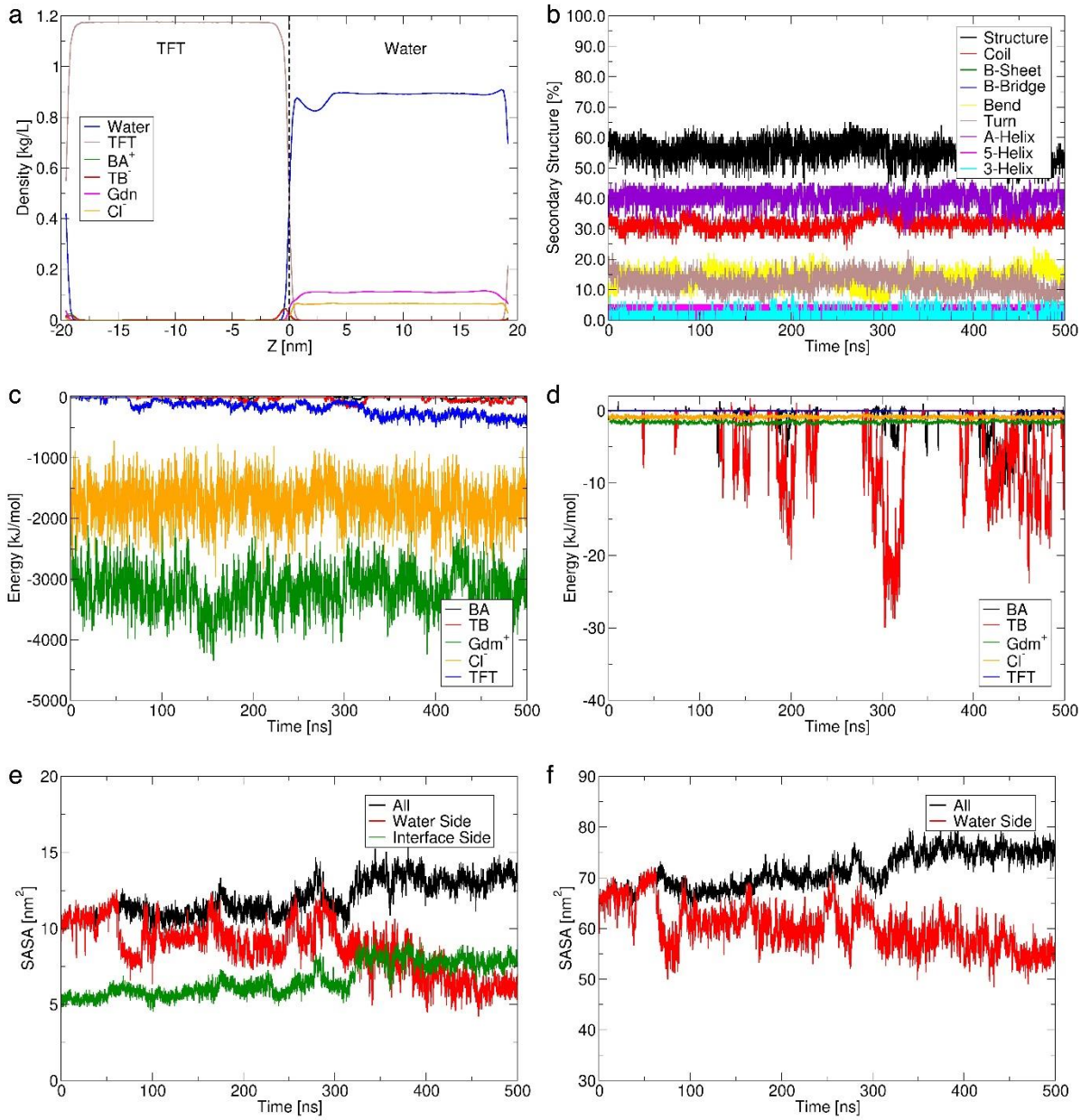

Fig. S19. Control simulation of Cyt *c* where Met-Heme bond is allowed to remain intact in the presence of GdmCl: (a) density profiles, (b) secondary structure, (c) interaction energies, (d) normalized interaction energies, (e) SASA due to hydrophobic residues, and (f) SASA.

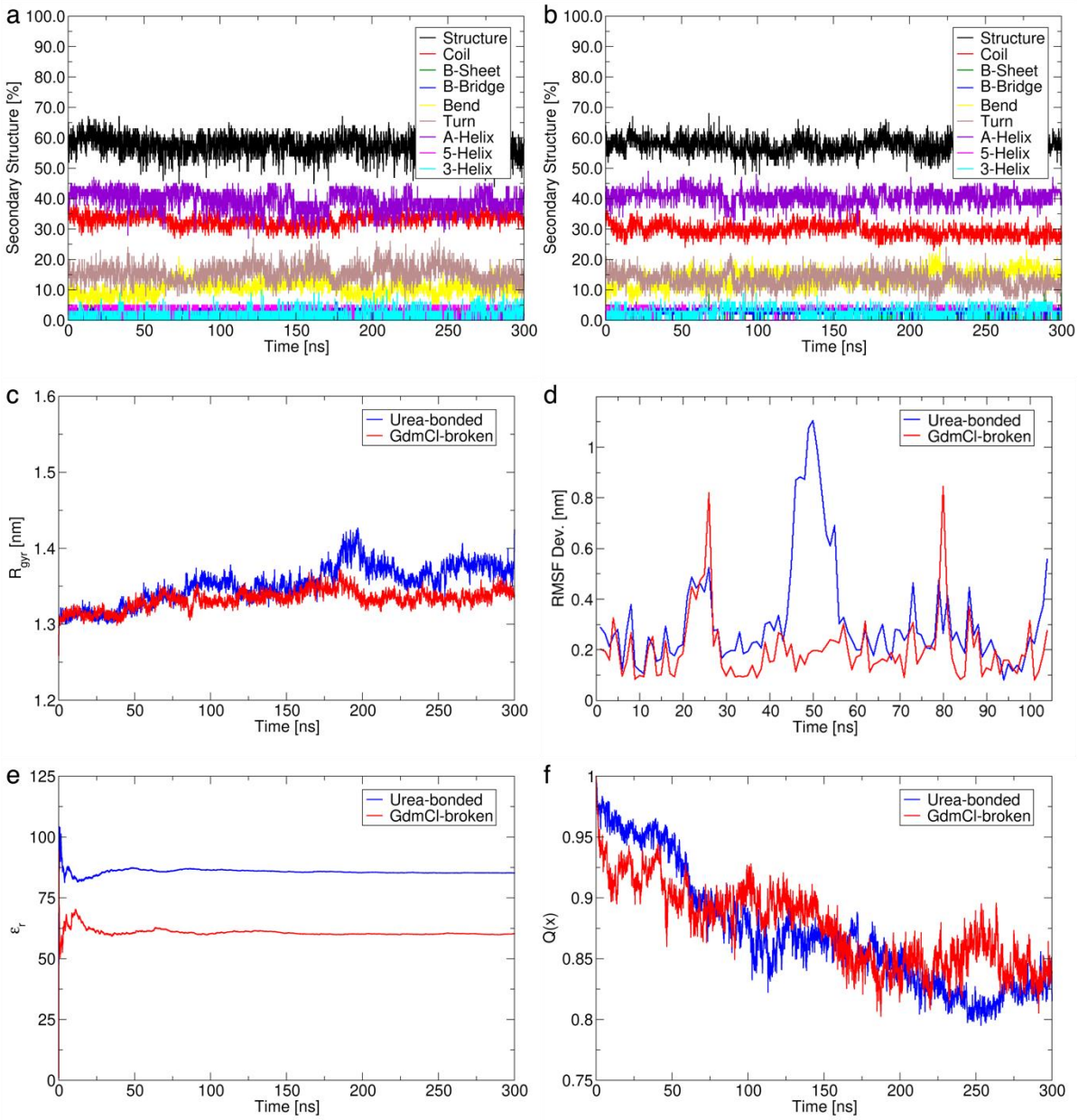

Fig. S20. Control simulations of Cyt *c* in a water box with no interface in the presence of Urea and GdmCl, respectively: (a) secondary structure of Cyt *c* with urea, (b) secondary structure of Cyt *c* with GdmCl, (c) radius of gyration (R_{gyr}), (d) deviation of the RMSF from initial structure, (e) relative dielectric constant, and (f) fraction of native contacts.

Supplementary references

1 M. F. Suárez-Herrera and M. D. Scanlon, *Electrochim. Acta*, 2019, **328**, 135110.

2 Z. Samec, *Pure Appl. Chem.*, 2004, **76**, 2147–2180.

3 Z. Samec, *Electrochim. Acta*, 2012, **84**, 21–28.

4 P. Peljo and H. H. Girault, in *Encyclopedia of Analytical Chemistry*, John Wiley & Sons, Ltd, Chichester, UK, 2012.

5 E. Smirnov, P. Peljo, M. D. Scanlon and H. H. Girault, *Electrochim. Acta*, 2016, **197**, 362–373.

6 A. Gamero-Quijano, G. Herzog and M. D. Scanlon, *Electrochem. commun.*, 2019, **109**, 106600.

7 P. Peljo, E. Vladimirova, E. Smirnov, G. Gschwend, L. Rivier and H. H. Girault, *J. Phys. Chem. C*, 2018, **122**, 18510–18519.

8 Y. Sun, V. Karunakaran and P. M. Champion, *J. Phys. Chem. B*, 2013, **117**, 9615–9625.

9 N. Mirkin, J. Jaconcic, V. Stojanoff and A. Moreno, *Proteins Struct. Funct. Bioinforma.*, 2007, **70**, 83–92.

10 Schrödinger Release 2021-2: Maestro, Schrödinger, LLC, New York, NY, 2021.

11 L. C. Petersen and R. P. Cox, *Biochem. J.*, 1980, **192**, 687–693.

12 D. Alvarez-Paggi, L. Hannibal, M. A. Castro, S. Oviedo-Rouco, V. Demicheli, V. Tórtora, F. Tomasina, R. Radi and D. H. Murgida, *Chem. Rev.*, 2017, **117**, 13382–13460.

13 J. Huang, S. Rauscher, G. Nawrocki, T. Ran, M. Feig, B. L. De Groot, H. Grubmüller and A. D. MacKerell, *Nat. Methods*, 2016, **14**, 71–73.

14 A. D. MacKerell, D. Bashford, M. Bellott, R. L. Dunbrack, J. D. Evanseck, M. J. Field, S. Fischer, J. Gao, H. Guo, S. Ha, D. Joseph-McCarthy, L. Kuchnir, K. Kuczera, F. T. K. Lau, C. Mattos, S. Michnick, T. Ngo, D. T. Nguyen, B. Prodhom, W. E. Reiher, B. Roux, M. Schlenkrich, J. C. Smith, R. Stote, J. Straub, M. Watanabe, J. Wiórkiewicz-Kuczera, D. Yin and M. Karplus, *J. Phys. Chem. B*, 1998, **102**, 3586–3616.

15 K. Kaszuba, P. A. Postila, O. Cramariuc, M. Sarewicz, A. Osyczka, I. Vattulainen and T. Róg, *Theor. Chem. Acc.*, 2013, **132**, 1–13.

16 B. Hess, H. Bekker, H. J. C. Berendsen and J. G. E. M. Fraaije, *J. Comput. Chem.*, 1997, **18**, 1463–1472.

17 S. Miyamoto and P. A. Kollman, *J. Comput. Chem.*, 1992, **13**, 952–962.

18 R. W. Hockney, *Methods Comput. Phys.*, 1970, **9**, 135–211.

19 T. Darden, D. York and L. Pedersen, *J. Chem. Phys.*, 1993, **98**, 10089–10092.

20 H. J. C. Berendsen, J. P. M. Postma, W. F. Van Gunsteren, A. Dinola and J. R. Haak, *J. Chem. Phys.*, 1984, **81**, 3684–3690.

21 W. Humphrey, A. Dalke and K. Schulten, *J. Mol. Graph.*, 1996, **14**, 33–38.

22 R. B. Best, G. Hummer and W. A. Eaton, *Proc. Natl. Acad. Sci. U. S. A.*, 2013, **110**, 17874–17879.

23 R. T. McGibbon, K. A. Beauchamp, M. P. Harrigan, C. Klein, J. M. Swails, C. X. Hernández, C. R. Schwantes, L. P. Wang, T. J. Lane and V. S. Pande, *Biophys. J.*, 2015, **109**, 1528–1532.

24 M. M. G. Krishna, Y. Lin, J. N. Rumbley and S. W. Englander, *J. Mol. Biol.*, 2003, **331**, 29–36.

25 A. I. Karsisiotis, O. M. Deacon, M. T. Wilson, C. Macdonald, T. M. A. Blumenschein, G. R. Moore and J. A. R. Worrall, *Sci. Rep.*, 2016, **6**, 30447.

26 M. E. P. Murphy, G. D. Brayer, J. S. Fetrow and R. E. Burton, *Protein Sci.*, 1993, **2**, 1429–1440.

27 P. Mulligan-Pullyblankt, J. S. Spitzer, B. M. Gilden and J. S. Fetrow, *J. Biol. Chem.*, 1996, **271**, 8633–8645.